crystals

MDPI

Article

High-Performance Zr-Doped P3-Type $Na_{0.67}Ni_{0.33}Mn_{0.67}O_2$ Cathode for Na-Ion Battery Applications

Sayoojyam Brahmanandan, Shantikumar Nair and Dhamodaran Santhanagopalan *

Amrita School of Nanosciences and Molecular Medicine, Amrita Vishwa Vidyapeetham, Kochi 682041, India
* Correspondence: dsgopalan20710@aims.amrita.edu

Abstract: Sodium-ion battery (SIB) technology started to bloom along with lithium-ion batteries (LIBs) as a supportive energy source to alleviate the cost of lithium sources for the development of energy storage devices and electric vehicles. Layered cathode materials are considered potential candidates to produce high-energy-density batteries. Among the layered cathode materials, P3-type cathodes are the least investigated in spite of their capacities, which are comparable to those of P2-type cathodes. P3-type cathodes show high polarization, leading to a poor cycle life, which impedes their extensive use in practical applications. In this work, we report on zirconium doping as an effective strategy to improve cycling stability and reduce voltage fading, another serious issue of layered cathode materials. It is found that an optimum composition of the P3-type cathode with Zr doping at the Mn site, leading to a composition of $Na_{0.67}Ni_{0.33}Mn_{0.64}Zr_{0.033}O_2$, shows good electrochemical performance in terms of retention (89% after 100 cycles) when compared to $Na_{0.67}Ni_{0.33}Mn_{0.60}Zr_{0.067}O_2$ (85% after 100 cycles) and an undoped sample (83% after 100 cycles). Also, remarkable performance is delivered by the $Na_{0.67}Ni_{0.33}Mn_{0.64}Zr_{0.033}O_2$ sample, with a retention rate of 72% after 450 cycles. This result is also supported by an analysis of the amount of polarization for undoped and doped samples, which found that doping helps in improving the diffusion of ions, and the least polarization is obtained for the $Na_{0.67}Ni_{0.33}Mn_{0.64}Zr_{0.033}O_2$ sample.

Keywords: P3-type layered cathode; metal oxide; Na-ion battery; doping; cycle life

check for updates

Citation: Brahmanandan, S.; Nair, S.; Santhanagopalan, D. High-Performance Zr-Doped P3-Type $Na_{0.67}Ni_{0.33}Mn_{0.67}O_2$ Cathode for Na-Ion Battery Applications. *Crystals* **2023**, *13*, 1339. https://doi.org/10.3390/cryst13091339

Academic Editors: Jianlin Li, Xiao-Guang Sun, Runming Tao, Cheng Li, Jiyuan Liang and Tianyu Zhang

Received: 31 July 2023
Revised: 21 August 2023
Accepted: 23 August 2023
Published: 1 September 2023

Copyright: © 2023 by the authors. Licensee MDPI, Basel, Switzerland. This article is an open access article distributed under the terms and conditions of the Creative Commons Attribution (CC BY) license (https://creativecommons.org/licenses/by/4.0/).

1. Introduction

The huge demand for energy consumption as part of the Industrial Revolution led to the depletion of non-renewable fossil fuel sources and augmented the emission of pollutants. Over the course of time, the development of renewable and clean energy sources like solar power, wind power, hydropower and geothermal and tidal energy gained attention. But the discontinuous nature of these resources limited their usage as steady sources. So, storing these energy resources and using them upon demand led to the necessity of energy conversion systems, such as fuel cells, water electrolysis, etc., and battery energy storage systems [1–4]. Batteries with high energy density are necessary for portable devices. Hence, the commercialization of lithium-ion batteries was started in 1991 by the Sony Corporation. As Li sources are limited, an alternate technology is required to meet the demands of electric vehicle (EV) and grid storage in the scenario of scaling up [5–8]. Due to the similar electrochemical properties exhibited by sodium ions, research on SIBs as a supporting source for lithium has also started along with LIBs. The abundant nature of sodium, the substitution of highly priced Cu foil with Al foil as current collector and the usage of electrolytes with cost-effective sodium salts are additional benefits. But compared with Li-ions, the size of Na-ions is high (1.02 Å), which can lead to a low practical capacity and poor rate capability for the same cathode material used in LIBs [5–10]. To attain batteries with high energy density, we require positive electrodes that show a high voltage as well as a high theoretical capacity. The cathode materials available for sodium-ion batteries include layered materials, polyanionic

compounds, organic compounds and Prussian blue analogues. Layered materials display a high theoretical capacity and high voltage. Also, layered cathode materials exhibit short ion diffusion paths and facile synthesis [11–13]. For the first time, Delmas et al. [14] investigated layered cathode materials for SIBs and suggested that the majority of the alkali metal ions crystallized into the layered cathode materials of the form Na_xMeO_2 (Me-redox-active transition metal), which was essentially confirmed by other research works [15,16]. Alternative Na and MeO_2 layers form the basic structure of these layered oxides. These layered oxides are classified as P (prismatic) and O (octahedral) depending on the co-ordination site occupied by Na ions between the MeO_2 layers. In O types, Na ions make contact with the MeO_6 octahedron along its edges, and diffusion occurs in the intermediate tetrahedral site. In the case of P types, diffusion is direct, and Na ions make contact with the MeO_6 octahedron along its edges as well as its faces. Based on the number of MeO_2 layers within a unit cell/the type of oxygen stacking, these layered oxides are classified as O3, O2, P3 and P2 [12,13]. The most widely studied, most stable types are P2 and O3, as they can be synthesized easily, and only recently, P3 joined the list. All these phases can be obtained via the sodium intercalation/de-intercalation process as well as by varying the calcination temperature, the gliding of MeO_2 layers and the breakage of Me-O, and by varying the sodium content [14–18]. Studies on Na_xMnO_2, first reported by Parant et al. [19], with different sodium concentrations, exhibited poor performance due to the Jahn–Teller effect exhibited by the Mn^{3+} ions. The moisture content in the atmosphere caused structural distortion in the case of $Na_{0.6}MnO_2$ [19–21]. New cathode materials exhibiting better performance were reported with the incorporation of binary transition metals. $LiNi_{1/2}Mn_{1/2}O_2$ is a widely studied cathode material for lithium-ion batteries, and is obtained via the ion exchange method from its sodium counterpart [22–26]. An in situ XRD study of P2-$Na_{2/3}[Mn_{2/3}\ Ni_{1/3}]O_2$ by Lu and Dahn [24] established the reversible migration of sodium ions. Also, a reversible phase transformation of P2-O2 occurs during cycling, with a first charge capacity of 161 mAh/g, which is close to the theoretical value of 173 mAh/g, within a voltage range of 2–4.5 V [24,27]. Based on the literature, it is evident that studies on P3-type materials are limited when compared to those on the O3 and P2 types. It is possible to synthesize P3-$Na_{2/3}[Mn_{2/3}Ni_{1/3}]O_2$ if we control the temperature within 700–750 °C [28–30]. When compared to P2-type materials, P3-type materials have large interlayer spacing and good sodium-ion diffusion [31]. The novel P3-$Na_{0.67}Ni_{0.2}Mn_{0.8}O_2$ synthesized by Jeong et al. [32] showed redox activity of oxygen when the voltage window was raised to 4.1 and 4.4 V, that delivered high charge capacities of 174 mAh/g and 204 mAh/g respectively. Li et al. [33] reported the reason behind the capacity fading during cycling in P3-$Na_{2/3}[Mn_{2/3}Ni_{1/3}]O_2$. It is mainly due to the preferred occupation of Na around the Ni site due to the ordered arrangement of Mn and Ni.

Though these layered materials exhibit a favorable capacity and diffusion, phenomena such as complex irreversible phase transformation, a moisture-sensitive nature, lattice deformities and a volume change during cycling act as stumbling blocks [13,31]. To minimize the challenges related to electrode materials, surface engineering strategies like structural designs or surface modifications have been employed in many cases. Surface modification strategies can be summarized as coating, doping, etching and passivation. The most commonly used modification technique is doping, as it inhibits irreversible phase transformation during cycling and improves performance [34–38]. Studies conducted by Wang et al. [39] on P3-$Na_{0.65}Ni_{0.25}Mn_{0.75}O_2$ through doping with F and B reveal that P3-O1 phase transformation is reduced via F doping, whereas, via B doping, a more stable P2 phase is obtained with good reversibility and less polarization. Following Mg doping at the Ni site of P3-$Na_{0.67}Ni_{0.33}Mn_{0.67}O_2$, Ya-Nan et al. [30] reported an air-stable, high-voltage material that showed a discharge capacity of 124 mAh/g and 78% retention after 100 cycles. To inhibit irreversible phase transition and to enhance Na+ ion diffusion in P2-$Na_{0.7}Mn_{0.75}Ni_{0.25}O_2$, Amedzo-Adore, Mawuse et al. designed an oxygen-deficient material with the reductive treatment of NH_4HF_2 [40]. With the aim of improving the cycling performance

and structural stability of P2- $Na_{0.8}Mn_{0.5}Fe_{0.5}O_2$, Yang, Junghoon et al. substituted some of the Fe^{2+} ions with electrochemically inactive Mg^{2+} ions, which also exhibited a smooth voltage profile [41].

Here, in our work, we systematically investigated Zr^{4+} doping in the redox-inactive Mn site of P3-type $Na_{0.67}Ni_{0.33}Mn_{0.67}O_2$. As the ionic radius of Zr^{4+} is larger than that of Mn^{4+}, lattice expansion-associated positive changes in electrochemical performance, such as improved cycling stability and a rate capability similar to that observed in Zr doping in Li-ion cathodes, may be expected [42–47].

2. Materials and Methods

We prepared the undoped $Na_{0.67}Ni_{0.33}Mn_{0.67}O_2$ (NNMO) sample and the different Zr concentrations (5 mol.% and 10 mol.% concentration of Mn) doped at the Mn site of the NNMO samples via typical sol gel synthesis. Here, 5 mol.% Zr, i.e., $Na_{0.67}Ni_{0.33}Mn_{0.637}Zr_{0.0335}O_2$, is indicated as NNMZr3O, and 10 mol%, i.e., $Na_{0.67}Ni_{0.33}Mn_{0.603}Zr_{0.067}O_2$, is indicated as NNMZr6O. Precursors such as sodium acetate (Sigma-Aldrich, Bengaluru, India), nickel (II) acetate tetra hydrate (98%, SRL Chem, Mumbai, India), manganese acetate tetra hydrate (99.0%, Sigma-Aldrich, Bengaluru, India) and zirconyl nitrate hydrate (25–30%, SRL Chem, Mumbai, India) were diluted independently in 10 mL of deionized water (DI) kept, in addition to the chelating agent citric acid monohydrate (extra pure, SRL Chem, Mumbai, India), in 5 mL DI at 40 °C. This was then added drop-wise to a beaker containing sodium acetate solution. After neutralization with ammonia solution (extra pure, AR, 25%, SRL Chem, Mumbai, India), it was stirred constantly over a hot plate at a temperature of 70 °C until we obtained a wet gel. Upon gelation, it was then subjected to air drying over night at 120 °C. The as-prepared sample was subjected to pre-calcination at 450 °C for 10 h with a ramp rate of 5 °C/min, starting at room temperature. Once it was cooled down to 70 °C, we ground it properly and calcined it at 750 °C for 10 h with a ramp rate of 5 °C/min in an air atmosphere.

Powder X-ray diffraction (XRD) of all the samples was performed using a 2nd generation D2 Phaser (Bruker, Karlsruhe, Germany), with a 2θ range of 10–70° and step size of 0.024°. With the default program in Bruker EVA, the removal of Cu K_α signals and background subtraction were performed. Rietveld refinement was carried out using the Profex program [48]. To analyze the phase transitions during cycling, ex situ XRD at the end of the first charge and at the end of the first cycle for all samples was performed and compared with the pristine electrode. Imaging of all samples with a high and low magnification was performed using transmission electron microscopy (TEM, JEM 2100 Jeol, Tokyo, Japan). For the surface analysis and the oxidation states of the powdered samples, X-ray photoelectron spectroscopy (XPS) was performed using an Al Kα monochromatic X-ray source with a power of 96 W and a beam spot size of 700 µm × 300 µm (Axis Ultra Kratos, Manchester, UK). The uniform elemental distribution of the samples was validated using field emission scanning electron microscopy (FESEM)–energy dispersive X-ray spectroscopy (EDS) analysis with 2D area mapping (JSM 7610 FPlus, Jeol, Tokyo, Japan).

To carry out the electrochemical study, positive electrodes were prepared using our active materials, multiwalled carbon nano-tubes (Reinste) and polyvinylidene fluoride (Sigma-Aldrich, Bengaluru, India), in a weight ratio of 80:10:10. Using 1-methyl 2 pyrolidone (anhydrous 99.5%, Sigma-Aldrich, Bengaluru, India) solvent, it was mixed properly, cast on Al foil and subjected to 15 min of drying in an IR lamp oven. Electrode discs with an area of 1 cm^2 and a loading of 2.5 mg cm^{-2} were punched out, and properly pressed on the foil using a hydraulic press. Half-inch-diameter Swagelok cells were assembled in an Ar-filled glove box (Unilab Pro, MBRAUN, Germany) with Na-metal as the anode and in-house-prepared 1M $NaClO_4$ in PC:VC (5 vol.%) as the electrolyte. Galvanostatic charge–discharge studies at different specific currents for all the samples were carried out in a potential range of 2.0–4.0 V (and 2.0–4.4 V) using BCS 805 (Biologic Instruments, Knoxville, TN, USA), and cyclic voltammetry (CV) data were also recorded using the same instrument. Electrochemical impedance spectroscopy (EIS) was performed under open

circuit voltage conditions with an ac amplitude of 10 mV in a frequency range of 10 mHz to 10 kHz using the BCS 805 instrument. For ex situ XRD, an analysis of the electrodes at the end of the first charge and at the end of the first discharge was carried out along with an analysis of the pristine electrodes for comparison. The charged and discharged cells were placed inside the glove box and the electrodes were washed with PC solvent to dissolve any salt residue on the surface and left inside the glove box to dry. Once dried, the electrodes were taken out for XRD measurement.

3. Results

3.1. Structure and Morphology

Figure 1a shows the XRD data obtained for the undoped and the Zr–doped NNMO samples that crystalized in the P3-type layered structure with a small concentration of P2-type impurity. All the well-defined sharp and intense peaks could be indexed on the basis of a hexagonal structure (R-3m space group). A shift of (003) peaks to the lower 2θ value is shown in Figure 1b due to Zr doping, which indicates lattice expansion and the successful incorporation of Zr^{4+} ions with larger ionic radii (0.72 Å) into the Mn^{4+} site (0.53 Å). To calculate the P2-type cathode phase fraction, Rietveld refinement was carried out on the NNMO sample. The result is displayed in Figure S1 and Table S1. It may be noted that the lattice parameter values of "a" and "c" are consistent with the literature values, whereas the P2-type cathode phase fraction was 14 wt.%. Figure 2a–c represent the low-magnification TEM images of the sample, in which the particles are of random shapes without proper facets for all three samples. From the HRTEM (Figure 2d–f) images, we can see lattice fringes with d-spacing values of 0.240, 0.246 and 0.244 nm for NNMO, NNMZr3O and NNMZr6O, respectively, which belong to the (012) lattice of the P3-type layered material with an R-3m space group [26,27,49]. The HRTEM-measured lattice spacing shows increase in d-spacing for the Zr-doped samples compared to the undoped NNMO sample is consistent with the XRD results.

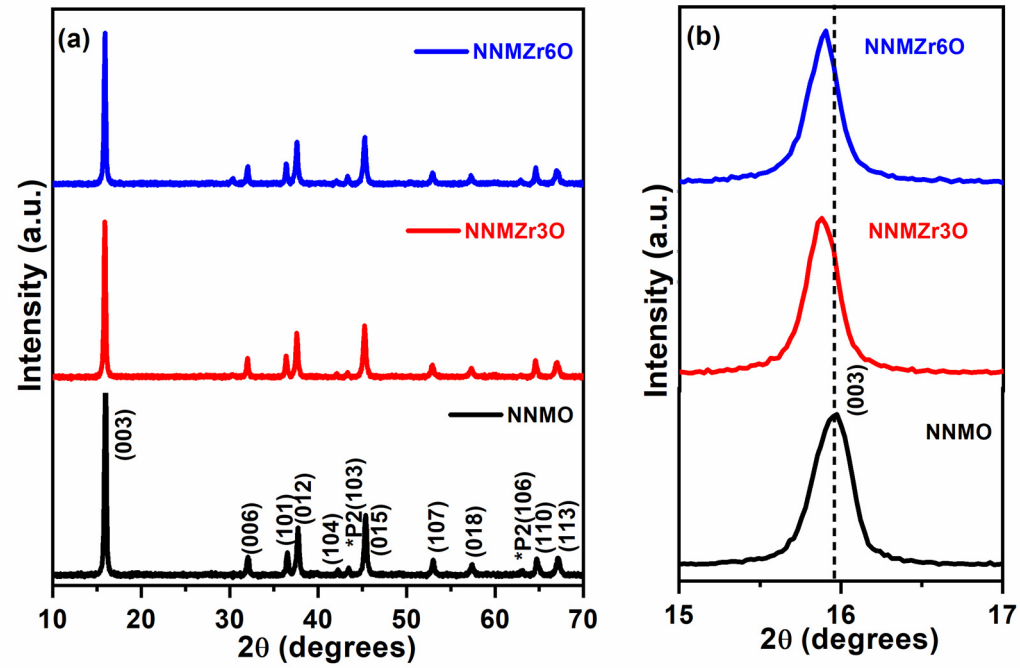


Figure 1. (**a**) XRD of the undoped and doped samples. (**b**) Displacement in peak position due to difference in ionic radii of Mn^{4+} and Zr^{4+}.

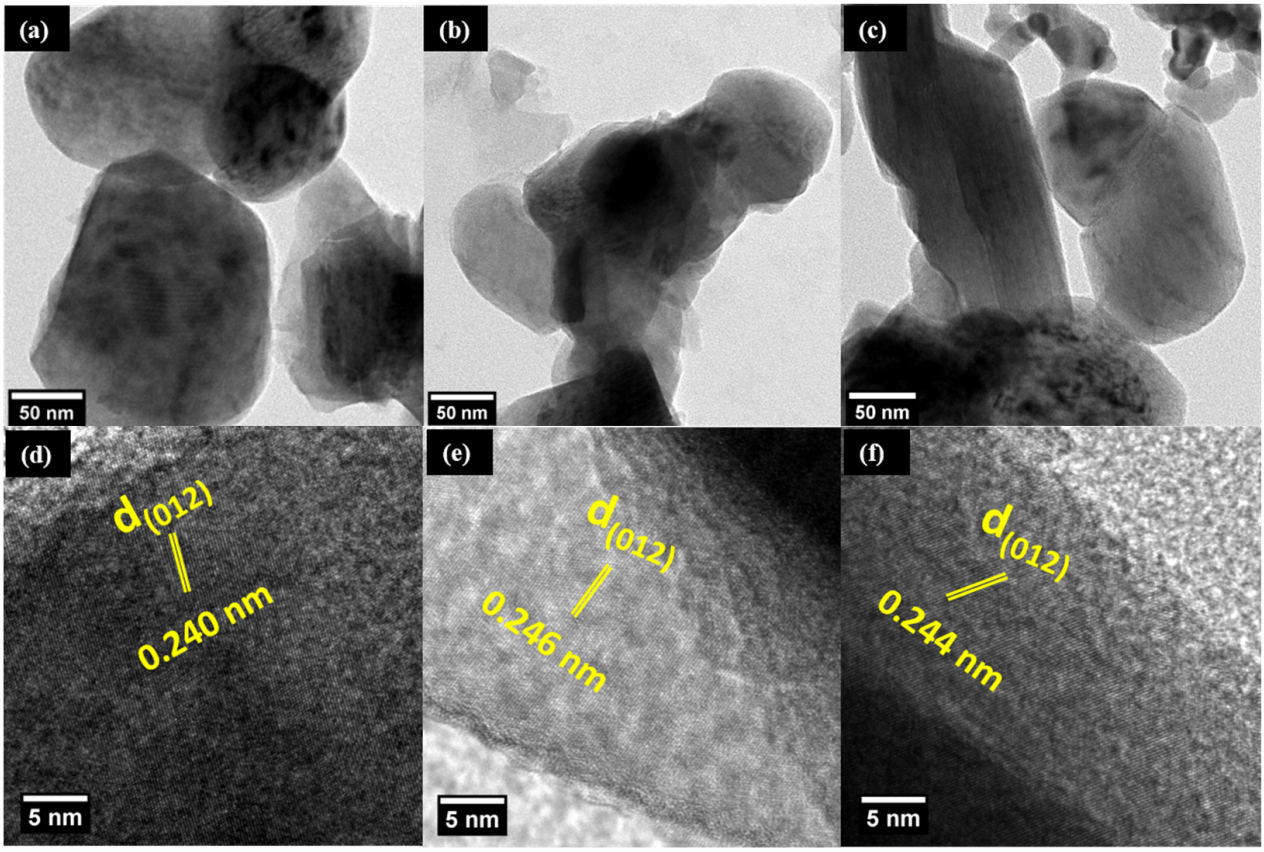


Figure 2. TEM images of (**a**–**c**) NNMO, NNMZr3O and NNMZr6O and (**d**–**f**) HRTEM images of the respective samples.

3.2. Surface Chemical Analysis

The XPS data of the undoped and doped samples are shown in Figure 3. Figure 3a shows a survey scan that suggests the presence of elements, namely, Na, Ni, Mn, Zr and O, as well as the reference C, and no other impurities. Figure 3b displays the high-resolution XPS spectra of C1s peaking at 284.6 eV (C-C) and a less intense peak at 288.6 eV (C=O) [47]. In Figure 3c, from the high-resolution O 1s data, an intense and broad peak at 529 eV originating from lattice oxygen is clearly seen [39,47,50–52]. The O 1s spectra of the doped samples show a minor shift towards higher binding energy. It may be noted that the overlap of lattice oxygen and surface hydroxyl groups can shift the peak towards higher binding energy. As the transition metal high-resolution spectra do not show any significant shifts, this overlap is possibly the reason for the O 1s peak shifts. Figure 3d shows the Na 1s spectra of the undoped and doped samples, with a binding energy value of nearly 1070 eV representing Na^+ [39]. From the XPS data for Ni 2p (Figure 3e), we can see the Ni (II) cations have peak positions at around 854 and 871 eV, while the Ni (III) cations have peak positions at 855.9 and 872.5 eV, respectively [39,44,50–54]. The binding energy values at 641 and 653 in Figure 3f show the presence of $2p_{3/2}$ and $2p_{1/2}$ in the Mn (III) cations, and for the Mn (IV) cations, the $2p_{3/2}$ and $2p_{1/2}$ binding energy values are 642.1 and 653.9 eV, respectively [39,50–54]. The characteristic peaks in Figure 3g at 181.9 eV and 184.2 eV belongs to Zr $3d_{5/2}$ and Zr $3d_{3/2}$, respectively; both are a clear indication of a Zr^{4+} oxidation state [44,53,54].

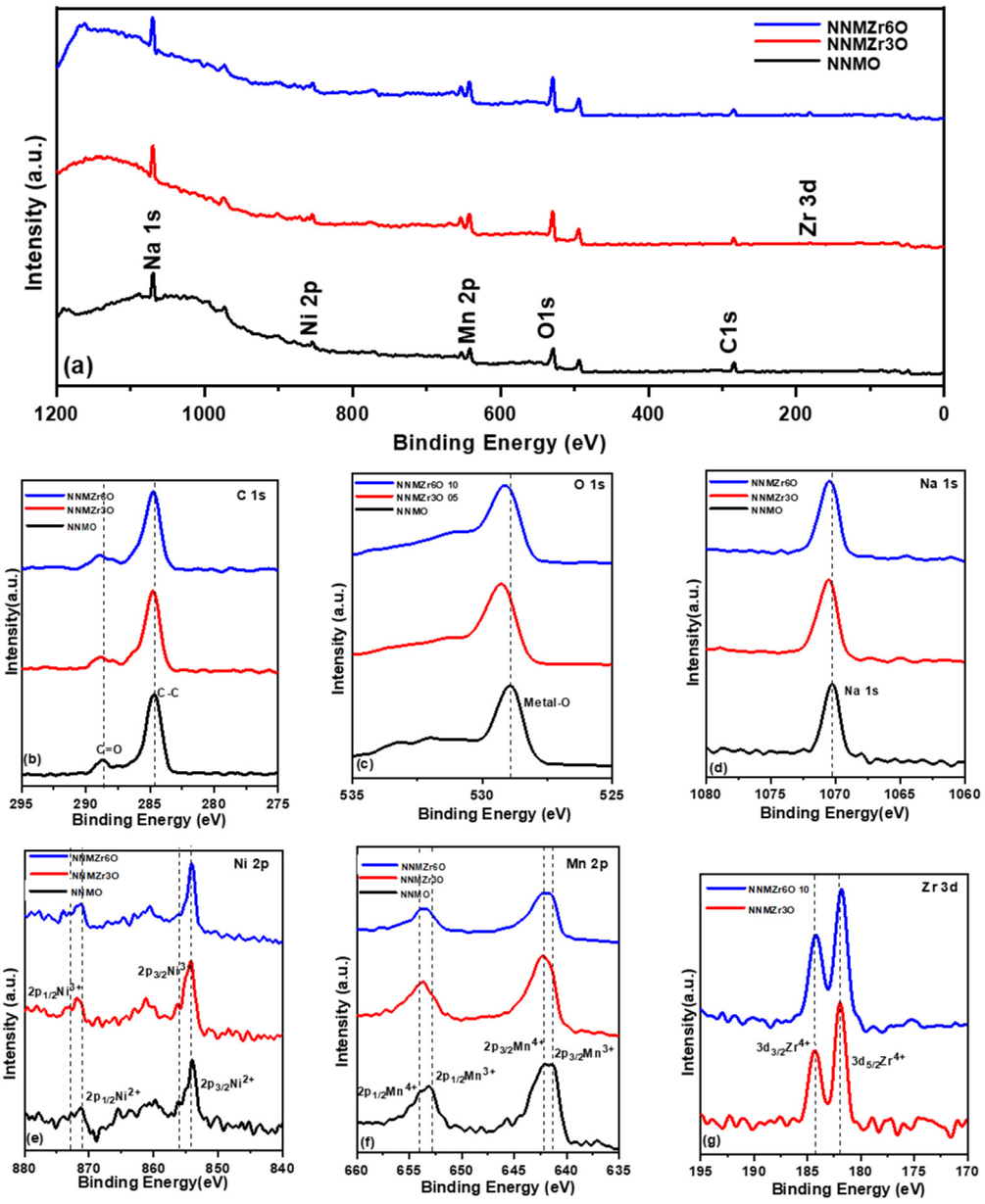


Figure 3. XPS spectra of undoped and Zr-doped NNMO samples. (**a**) Survey, (**b**) C1s, (**c**), O 1s, (**d**) Na 1s, (**e**) Ni 2p, (**f**) Mn 2p and (**g**) Zr 3d.

3.3. Electrochemical Investigations

To investigate the redox processes in the undoped and doped samples, cyclic voltammetry (CV) measurements of all three samples were taken. Figure S3 shows the CV profiles of the samples at a scan rate of 0.1 mV/s for three cycles between 2 and 4 V. From the figure, it is clear that there are four major peaks within the cycled voltage limits, which confirms the ordering of Na^+/vacancy [30,41,55]. The peaks obtained between the voltage regions of 3and 4 V correspond to the Ni^{2+}-Ni^{4+} reversible redox couple, whereas the ones below 3V are contributed by Mn^{3+}/Mn^{4+} [30,34,55]. The CV profiles of the undoped and doped samples imply that through doping, structural stability is attained during cycling, which is indicated by the overlapping oxidation peaks of the doped samples at ~3.7 V. Further, it is seen that structural reconstruction happens in the first few cycles for all the samples, as demonstrated by the reduction peak position at ~3.37 V, which becomes less prominent after few cycles. In the charge–discharge study shown in Figure 4, this surface reconstruction is visible as a small plateau at 3.4 V for all samples that vanishes after few

cycles. From the area under the CV profiles, NNMZr6O exhibits the lowest value, which implies a low capacity, consistent with the galvanostatic charge–discharge data of NNMZr6O. Figure 4a–c shows the charge–discharge profile of undoped and doped samples cycled at 50 mA/g, within a voltage window of 2–4 V for the 1st, 25th, 50th and 100th cycles. For all the samples, a clear step-like, prolonged plateau region is obtained during charging, which is the due to the oxidation of $Ni^{2+}/^{3+}/^{4+}$, with an average potential ≥3.2 V [49,54,55]. The plateau indicates the formation of a biphasic system during sodiation/desodiation. A major portion of Mn will be in the redox-inactive 4+ state, and a small portion will be in the active 3+ state. As mentioned above, a small step-like feature is visible around 3.4 V in the first discharge, which fades away as cycling proceeds.

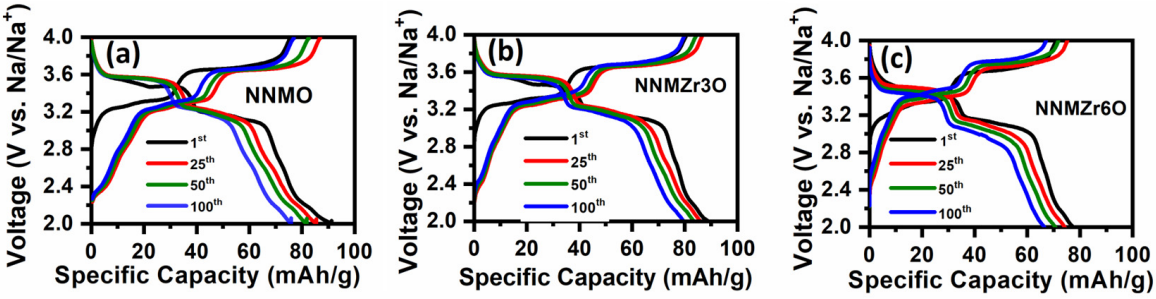


Figure 4. Charge–discharge studies of (**a**) NNMO, (**b**) NNMZr3O and (**c**) NNMZr6O for same current density of 50 mA/g.

Figure S4 shows the charge–discharge profiles of all the three samples with the same condition as shown in Figure 4 but at one particular cycle for comparison. We can see the effect of doping on voltage polarization in these three samples, which will further affect Na^+ ion diffusion. It is clearly visible from the profile that doping helped in decreasing voltage polarization and improving the diffusion process of the doped samples compared to the NNMO sample. Further, NNMZr3O exhibits the least polarization, which is also confirmed by the retention study and differential capacity analysis, which will be discussed later.

Figure 5a shows the rate capability of the undoped and doped samples for current densities of 25, 50, 75, 100 and back to 25 mA/g, with five cycles at each step. The Zr–doped sample, i.e., NNMZr3O (NNMZr6O), displays capacities of 87.3 (81.2), 83.4 (77.5), 80.9 (75.4) and 79.3 (73.8) mAh/g for current densities of 25, 50, 75 and 100 mA/g, respectively, with a retention rate of 90%, and when again cycled back to 25 mA/g, shows a retention rate of 97% compared to the first cycle. Meanwhile, NNMO displays capacities of 92, 85.6, 77 and 73.8 mAh/g for current densities from 25 to 100 mA/g, with a 75% retention rate, and when cycled back to 25 mA/g, shows 89% retention. From the cycling study performed for the undoped and doped samples (Figure 5b), the undoped sample has an initial discharge capacity of 91.3 mA/g, which reduces to 75.9 mA/g with a retention rate of 83.2% after 100 cycles. In the case of NNMZr3O, even though the initial discharge capacity of 89 mAh/g is slightly lower compared to the undoped sample, it exhibits a retention rate of 89.4% after 100 cycles. For the NNMZr6O sample, the initial discharge capacity is less than half of the capacity of the NNMO sample but shows a retention rate of 85.6% after 100 cycles. From the data obtained, we can see that only an optimum concentration of Zr doping in the Mn site helps in cycling stability, while increasing the doping concentration cannot enhance Na-ion diffusion effectively, which results in lower discharge capacity. The excess Zr^{4+} ions may become trapped within the crystal structure, and thus, do not take part in interlayer expansion. Figure 5c represents the long cycling data of NNMZr3O for 450 cycles, with a good capacity retention of 72%. This result shows that Zr doping helps in stabilizing the cycle life of P3-NNMO.

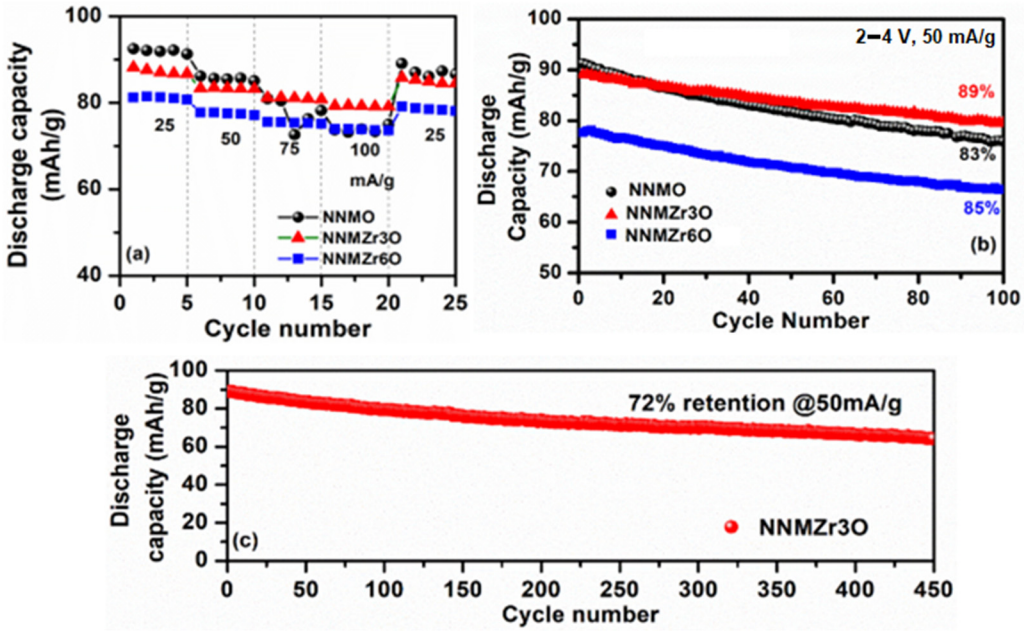


Figure 5. (**a**) Rate performance of NNMO, NNMZr3O and NNMZr6O. (**b**) Cycling data of NNMO, NNMZr3O and NNMZr6O. (**c**) Long cycling performance of NNMZr3O.

Figure 6a–c displays the first-cycle charge–discharge profiles of the undoped and doped samples at different current densities of 25, 50, 75 and 100 mA/g for a voltage range of 2.0–4.0 V. From the profiles, we can clearly see the low polarization and improvement in capacity at high rates for the NNMZr3O sample compared to NNMO. Figure 6d–f depict the differential capacity analysis of the corresponding data in Figure 6a–c at different current densities. From the analysis, three pairs of redox peaks are noted within 2.5–4 V, demonstrating the three voltage plateaus corresponding to the phase transition that happens during cycling. The redox couple obtained for samples cycled in a voltage window of 2–4 V @25 mA/g is listed in Table S2. Similar peak positions are observed in the CV analysis of all samples, revealing the $Ni^{2+/3+/4+}$ redox couple for the region between 3 and 4 V. In a more recent study conducted by Zhou, Ya-Nan et al. [36] in suppressing the phase transition of P3–NNMO via local symmetry tuning, the authors mentioned the ordering of Na+/vacancy and a P3–O3 phase transition in the voltage regions of 3.1–3.3 V and 3.5–3.7 V, respectively. For the undoped samples, the position of peaks obtained as we increase the current density shifts towards right/left during charging/discharging, which is an indication of higher voltage polarization. Meanwhile, in the case of doped samples, the positions of the peaks overlap on top of each other, even during the increased current density, which indicates reduced polarization as well as good structural stability [54]. Voltage polarization is an indication of the rate limiting step via a charge pile-up at the electrode–electrolyte interface [56–58]. The quantified charge–discharge voltage polarization values as a function of current density are shown in Figure 6g. It is observed that polarization is diminished, possibly due to the elevated interface kinetics. Among the doped samples, NNMZr3O shows less polarization, which is in agreement with the result obtained from the retention rate analysis discussed earlier. Also, we evaluated the capacity contribution from each plateau as we increased the current density for the undoped and doped samples, which is shown in Figure 6h. In the case of the undoped sample, it is observed that as we increase the current density, the capacity contribution by the first plateau decreases, which affects the total capacity delivered by the sample, whereas, for doped samples, this effect is not observed, and hence, they deliver more or less same capacity as at a higher current density. The decreasing first plateau capacity of the undoped sample is an indication of the loss of Ni^{2+}, which could be due to disorder-induced cation mixing. Such mixing is possibly

suppressed by Zr doping, as observed, to maintain the plateau capacity for both of the doped NNMO samples.

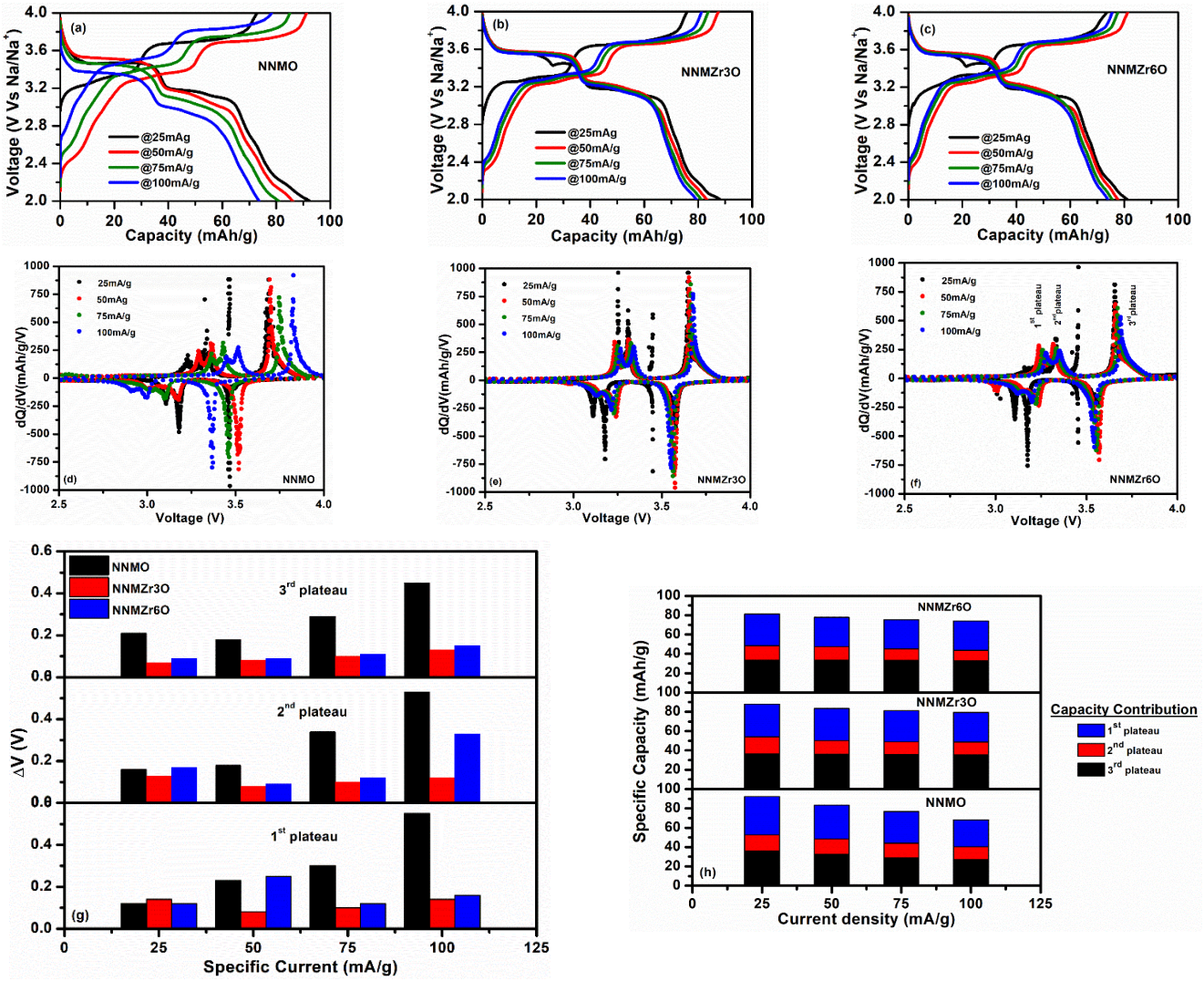


Figure 6. (**a**–**c**) Charge–discharge investigations at different rates: (**d**–**f**) differential profiles of undoped and Zr-doped NNMO samples, (**g**) rate-dependent voltage polarization and (**h**) capacity contribution of different plateaus.

Figure S5 shows the electrochemical impedance spectroscopy data of the undoped and Zr-doped samples under open circuit voltage (OCV) conditions. It is clear that the spectra show two semi-circles at high- and mid-frequency ranges, with the first semi-circle occurring due to any distinct surface layer (such as the solid-electrolyte interfacial layer or chemically/structurally different layers) and second semi-circle due to charge transfer resistance. A short straight line in the low-frequency region and its slope correspond to the diffusion kinetics of the ions. Based on the impedance spectra of all the three samples, under OCV conditions, high charge transfer resistance for NNMZr3O and the least resistance for the NNMZr6O sample can be noted (though the series resistance values of all three samples are similar). This could be correlated with the differences in the surface structure of the samples as surface reconstruction was observed during the first few cycles of the high-voltage plateaus of all three samples, for which the individual plateau length and the surface reconstruction responsible need to be investigated. It was not the main aim of the present work to explore this mechanism, and hence, detailed correlative electrochemistry–microscopy at different stages of charge–discharge is required in the future.

To study the phase transition mechanism of the three samples (NNMO, NNMZr3O and NNMZr6O), ex situ XRD of the electrodes was performed before and after cycling (at the end of first charge and first discharge) and the data are shown in Figures S6–S8. The XRD obtained for the pristine electrodes of all three samples matches with the result obtained for the powder XRD samples (in Figure 1a), with additional peaks appearing from the Al-foil (the peak at 64.3° was utilized for calibration). For all the samples in their charged state, two hydrated peaks are found at around 12° and 25°, which is due to the intercalation of water molecules in the layered material due to the presence of Na+ ion vacancies and the widened gap between layers; this is consistent with the ex situ XRD observations of layered cathodes in the charged state reported in the literature [11,21,30]. After charging (i.e., desodiation) the layered structure becomes unstable and water molecules can easily become trapped, which leads to such a hydrated phase. In the XRD pattern of NNMZr3O charged electrodes, a small intense peak of ZrO_2 at 28.1° appears, which vanishes after discharging. This oxide peak of zirconium is not visible in the charged electrode of the NNMZr6O sample, but appears in the discharged electrode; the reason is not clear at the moment. An additional peak at 50° is observed in all electrodes in their charged state, the reason for which is also unidentified. While analyzing the XRD data of the discharged samples, we found that the peaks obtained match with the pristine electrodes of all the respective samples, which suggests a reversible phase transition after discharging down to 2.0 V. However, a significant peak shift to lower 2θ values for all the samples is noted, and the peak shift is at maximum for the NNMZr3O sample and minimal for undoped NNMO sample. Such a peak shift to a lower angle indicates a lattice expansion at the end of the first discharge relative to the pristine electrodes (while the Al-foil peak is matched properly without any shift). Such an expansion would help in improving Na diffusion in the doped samples. This could be the possible reason for the improved performance of the NNMZr3O sample compared to the undoped NNMO sample. However, more detailed in situ XRD data or ex situ data after long cycling would be required to provide a solid conclusion.

The high-voltage performance of these samples was measured to analyze their cycling stability in a potential window of 2–4.4 V. At a current density of 50 mA/g for 50 cycles, the data are shown in Figure S9a–d. When cycled up to 4.4 V, NNMO, NNMZr3O and NNMZr6O deliver initial discharge capacities of 158, 152 and 147 mAh/g, respectively. The charge–discharge profile of the NNMO sample (Figure S9a) shows a prolonged plateau at around 4.25 V, which could be due to the P3–O3′ transition happening in the P3-layered cathode materials. But even after doping with zirconium, this prolonged plateau remains unchanged in the doped samples. But as the cycling proceeds, the plateau profile is transformed to a smooth curve at higher voltages, indicating the occurrence of a solid-solution-like mechanism. For analyzing the retention maintained at a high voltage of the undoped and doped samples, the cycling performance of 50 cycles was evaluated, as shown in Figure S9d. The data reveal poor capacity retention of about 40% for all three samples.

4. Conclusions

The layered cathode materials of a Na-ion battery have the potential to provide high capacity and high reduction potential. Layered cathode materials have a poor cycle life, and here, we adopted a bulk doping strategy to study the cycling stability and voltage fading issue exhibited by P3-type cathode materials. For this, we doped different concentrations of isovalent zirconium at the Mn site of an NNMO sample. The XRD finding shows expansion of the (003) interlayer spacing because of doping, which can improve cycling. Electrochemical analysis was performed in a safe voltage window of 2.0–4.0 V @ 50 mA/g for 100 cycles. It is found that the NNMZr3O sample shows better retention of 89% when compared to the undoped NNMO sample, which exhibits a retention rate of only 83% after 100 cycles. Also, it is found that only the optimum concentration of $Na_{0.67}Ni_{0.33}Mn_{0.64}Zr_{0.033}O_2$ helps in stabilizing the cycle life, when compared with the $Na_{0.67}Ni_{0.33}Mn_{0.603}Zr_{0.067}O_2$ sample. The long cycling data of NNMZr3O show 72% retention after 450 cycles, which also supports our findings. From the differential capacity analysis obtained for all samples, it is clear that

doping helped in reducing the polarization caused by the accumulation of charges due to an inadequate amount of sodium ions. The performance of the undoped and doped samples was analyzed in a high charge cut-off voltage range up to 4.4 V @50 mA/g; the results show a poor capacity retention of 39–40% for the three samples. This indicates that a more significant surface engineering process is necessary to improve the performance at high cut-off voltages.

Supplementary Materials: The following supporting information can be downloaded at: https://www.mdpi.com/article/10.3390/cryst13091339/s1, Figure S1: XRD refinement data; Figure S2: FESEM-EDS mapping data; Figure S3: Cyclic voltammetry data; Figure S4: Charge–discharge profiles for 2–4 V; Figure S5: Electrochemical impedance data; Figures S6–S8: Ex situ XRD data of all three samples; Figure S9: Charge–discharge profiles and cycling data of all three samples for 2–4.4 V window; Table S1: XRD refinement summary; Table S2: redox voltage value summary for all three samples in the voltage window of 2–4 V.

Author Contributions: Conceptualization and methodology, D.S.; validation, formal analysis and investigation, S.B.; resources, S.N.; data curation, S.B.; writing—original draft preparation, S.B.; writing—review and editing, D.S. and S.N.; supervision, D.S.; project administration, D.S.; funding acquisition, S.N. All authors have read and agreed to the published version of the manuscript.

Funding: This research was funded by the Department of Science and Technology, India, grant number DST/TMD/MES/2K18/225.

Data Availability Statement: The data are contained within the article or supplementary material.

Conflicts of Interest: The authors declare no conflict of interest.

References

1. Sun, H.; Song, S.; Xu, X.; Dai, J.; Yu, J.; Zhou, W.; Shao, Z.; Jung, W. Recent Progress on Structurally Ordered Materials for Electrocatalysis. *Adv. Energy Mater.* **2021**, *11*, 2101937. [CrossRef]
2. Sun, H.; Xu, X.; Song, Y.; Zhou, W.; Shao, Z. Designing High-Valence Metal Sites for Electrochemical Water Splitting. *Adv. Funct. Mater.* **2021**, *31*, 2009779. [CrossRef]
3. Olabi, A.G.; Onumaegbu, C.; Wilberforce, T.; Ramadan, M.; Abdelkareem, M.A.; Al-Alami, A.H. Critical Review of Energy Storage Systems. *Energy* **2021**, *214*, 118987. [CrossRef]
4. Hossain, E.; Faruque, H.M.R.; Sunny, M.S.H.; Mohammad, N.; Nawar, N. A Comprehensive Review on Energy Storage Systems: Types, Comparison, Current Scenario, Applications, Barriers, and Potential Solutions, Policies, and Future Prospects. *Energies* **2020**, *13*, 3651. [CrossRef]
5. Yang, L.; Brehm, W. From Lithium-Ion to Sodium-Ion Batteries: Advantages, Challenges, and Surprises. *Angew. Chem. Int. Ed.* **2017**, *57*, 102–120. [CrossRef]
6. Liu, G.; Sun, Z.; Shi, X.; Wang, X.; Shao, L.; Liang, Y.; Lu, X.; Liu, J.; Guo, Z. 2D-Layer-Structure Bi To Quasi-1D-Structure $NiBi_3$: Structural Dimensionality Reduction to Superior Sodium and Potassium Ion Storage. *Adv. Mater.* **2023**, 230551. [CrossRef]
7. Liang, Y.; Chen, Y.; Ke, X.; Zhang, Z.; Wu, W.; Lin, G.; Zhou, Z.; Shi, Z. Coupling of Triporosity and Strong Au-Li Interaction to Enable Dendrite-Free Lithium Plating/Stripping for Long-Life Lithium Metal Anodes. *J. Mater. Chem. A* **2020**, *8*, 18094–18105. [CrossRef]
8. Liu, G.; Wang, N.; Qi, F.; Lu, X.; Liang, Y.; Sun, Z. Novel Ni-Ge-P Anodes for Lithium-Ion Batteries with Enhanced Reversibility and Reduced Redox Potential. *Inorg. Chem. Front.* **2022**, *10*, 699–711. [CrossRef]
9. Abraham, K.M. How Comparable Are Sodium-Ion Batteries to Lithium-Ion Counterparts? *ACS Energy Lett.* **2020**, *5*, 3544–3547. [CrossRef]
10. Tapia-Ruiz, N.; Armstrong, A.R.; Alptekin, H.; Amores, M.A.; Au, H.; Barker, J.; Boston, R.; Brant, W.R.; Brittain, J.M.; Chen, Y.; et al. 2021 Roadmap for Sodium-Ion Batteries. *J. Phys. Energy* **2021**, *3*, 031503. [CrossRef]
11. Xiao, J.; Li, X.; Tang, K.; Wang, D.; Long, M.; Gao, H.; Chen, W.; Liu, C.; Liu, H.; Wang, G. Recent Progress of Emerging Cathode Materials for Sodium Ion Batteries. *Mater. Chem. Front.* **2021**, *5*, 3735–3764. [CrossRef]
12. Mauger, A.; Julien, C.M. State-of-the-Art Electrode Materials for Sodium-Ion Batteries. *Materials* **2020**, *13*, 3453. [CrossRef] [PubMed]
13. Wei, F.; Zhang, Q.; Zhang, P.; Tian, W.; Dai, K.; Zhang, L.; Mao, J.; Shao, G. Review—Research Progress on Layered Transition Metal Oxide Cathode Materials for Sodium Ion Batteries. *J. Electrochem. Soc.* **2021**, *168*, 050524. [CrossRef]
14. Delmas, C.; Fouassier, C.; Hagenmuller, P. Structural Classificatoin and Properties of the Layered Oxides. *Physica B Condens. Matter* **1980**, *99*, 81–85. [CrossRef]
15. Peng, B.; Sun, Z.; Zhao, L.; Zeng, S.; Zhang, G. Shape-Induced Kinetics Enhancement in Layered P2-$Na_{0.67}Ni_{0.33}Mn_{0.67}O_2$ Porous Microcuboids Enables High Energy/Power Sodium-Ion Full Battery. *Batter. Supercaps* **2021**, *4*, 388. [CrossRef]

16. Delmas, C. Sodium and Sodium-Ion Batteries: 50 Years of Research. *Adv. Energy Mater.* **2018**, *8*, 1–9. [CrossRef]
17. Liu, Y.; Liu, X.; Wang, T.; Fan, L.Z.; Jiao, L. Research and Application Progress on Key Materials for Sodium-Ion Batteries. *Sustain. Energy Fuels* **2017**, *1*, 986–1006. [CrossRef]
18. Yabuuchi, N.; Kubota, K.; Dahbi, M.; Komaba, S.N. Research Development on Sodium-Ion Batteries. *Chem. Rev.* **2014**, *114*, 11636–11682. [CrossRef]
19. Parant, J.; Olazcuaga, R.; Hagenmuller, P. Sur Quelques Nouvelles Phases de Formule Na_xMnO_2 ($x \leq 1$). *J. Solid State Chem.* **1971**, *3*, 1–11. [CrossRef]
20. Clément, R.J.; Bruce, P.G.; Grey, C.P. Review—Manganese-Based P2-Type Transition Metal Oxides as Sodium-Ion Battery Cathode Materials. *J. Electrochem. Soc.* **2015**, *162*, A2589–A2604. [CrossRef]
21. Caballero, A.; Hernán, L.; Morales, J.; Sánchez, L.; Santos Peña, J.; Aranda, M.A.G. Synthesis and Characterization of High-Temperature Hexagonal P2-$Na_{0.6}$ MnO_2 and Its Electrochemical Behaviour as Cathode in Sodium Cells. *J. Mater. Chem.* **2002**, *12*, 1142–1147. [CrossRef]
22. Lu, Z.; Donaberger, R.A.; Dahn, J.R. Superlattice Ordering of Mn, Ni, and Co in Layered Alkali Transition Metal Oxides with P2, P3, and O3 Structures. *Chem. Mater.* **2000**, *12*, 3583–3590. [CrossRef]
23. Paulsen, J.M.; Dahn, J.R. Studies of the Layered Manganese Bronzes, $Na_{2/3}[Mn_{1-x}M_x]O_2$ with M = Co, Ni, Li, and $Li_{2/3}[Mn_{1-x}M_x]O_2$ Prepared by Ion-Exchange. *Solid State Ion.* **1999**, *126*, 3–24. [CrossRef]
24. Lu, Z.; Dahn, J.R. In Situ X-ray Diffraction Study of P2-$Na_{2/3}Ni_{1/3}Mn_{2/3}O_2$. *J. Electrochem. Soc.* **2001**, *148*, A1225. [CrossRef]
25. Paulsen, J.M.; Larcher, D.; Dahn, J.R. O2 Structure $Li_{2/3}[Ni_{1/3}Mn_{2/3}]O_2$: A New Layered Cathode Material for Rechargeable Lithium Batteries I. Electrochemical Properties. *J. Electrochem. Soc.* **2000**, *147*, 861–868. [CrossRef]
26. Paulsen, J.M.; Larcher, D.; Dahn, J.R. O2 Structure $Li_{2/3}[Ni_{1/3}Mn_{2/3}]O_2$: A New Layered Cathode Material for Rechargeable Lithium Batteries II. Structure, Composition and Properties. *J. Electrochem. Soc.* **2000**, *147*, 2478–2485. [CrossRef]
27. Wang, S.; Sun, C.; Wang, N.; Zhang, Q. Ni- and/or Mn-Based Layered Transition Metal Oxides as Cathode Materials for Sodium Ion Batteries: Status, Challenges and Countermeasures. *J. Mater. Chem. A* **2019**, *7*, 10138–10158. [CrossRef]
28. Paulsen, J.M.; Donaberger, R.A.; Dahn, J.R. Layered T2-, O6-, O2-, and P2-Type $A_{2/3}[M'^{2+}{}_{1/3}M^{4+}{}_{2/3}]O_2$ Bronzes, A = Li, Na; M′ = Ni, Mg; M = Mn, Ti. *Chem. Mater.* **2000**, *12*, 2257–2267. [CrossRef]
29. Kalapsazova, M.; Ortiz, G.F.; Tirado, J.L.; Dolotko, O.; Zhecheva, E.; Nihtianova, D.; Mihaylov, L.; Stoyanova, R. P3-Type Layered Sodium-Deficient Nickel-Manganese Oxides: A Flexible Structural Matrix for Reversible Sodium and Lithium Intercalation. *Chempluschem* **2015**, *80*, 1642–1656. [CrossRef]
30. Zhou, Y.-N.; Wang, P.-F.; Zhang, X.-D.; Huang, L.-B.; Wang, W.-P.; Yin, Y.-X.; Xu, S.; Guo, Y.-G. Air-Stable and High-Voltage Layered P3-Type Cathode for Sodium-Ion Full Battery. *ACS Appl. Mater. Interface* **2019**, *11*, 24184–24191. [CrossRef]
31. Shi, C.; Wang, L.; Chen, X.; Li, J.; Wang, S.; Wang, J.; Jin, H. Challenges of layer-structured cathodes for sodium-ion batteries. *Nanoscale Horizons* **2022**, *7*, 338–351. [CrossRef] [PubMed]
32. Kim, E.J.; Ma, L.A.; Duda, L.C.; Pickup, D.M.; Chadwick, A.V.; Younesi, R.; Irvine, J.T.S.; Robert Armstrong, A. Oxygen Redox Activity through a Reductive Coupling Mechanism in the P3-Type Nickel-Doped Sodium Manganese Oxide. *ACS Appl. Energy Mater.* **2020**, *3*, 184–191. [CrossRef]
33. Zhang, L.; Wang, J.; Li, J.; Schuck, G.; Winter, M.; Schumacher, G.; Li, J. Preferential Occupation of Na in P3-Type Layered Cathode Material for Sodium Ion Batteries. *Nano Energy* **2020**, *70*, 104535. [CrossRef]
34. Anilkumar, A.; Nair, N.; Nair, S.; Baskar, S. Tailoring high Na content in P2-type layered oxide cathodes via Cu-Li dual doping for sodium-ion batteries. *J. Energy Storage* **2023**, *72*, 108291. [CrossRef]
35. Liu, Y.; Liao, J.; Tang, Z.; Chao, Y.; Chen, W.; Wu, X.; Wu, W. Improved Sodium Storage Performance of Zn-Substituted P3-$Na_{0.67}Ni_{0.33}Mn_{0.67}O_2$ Cathode Materials for Sodium-Ion Batteries. *J. Electron. Mater.* **2023**, *52*, 864–876. [CrossRef]
36. Zhou, Y.N.; Xiao, Z.; Han, D.; Wang, S.; Chen, J.; Tang, W.; Yang, M.; Shao, L.; Shu, C.; Hua, W.; et al. Inhibition of the P3-O3 Phase Transition via Local Symmetry Tuning in P3-Type Layered Cathodes for Ultra-Stable Sodium Storage. *J. Mater. Chem. A* **2023**, *11*, 2618–2626. [CrossRef]
37. Liu, Q.; Hu, Z.; Zou, C.; Jin, H.; Wang, S.; Li, L. Structural Engineering of Electrode Materials to Boost High-Performance Sodium-Ion Batteries. *Cell Rep. Phys. Sci.* **2021**, *2*, 100551. [CrossRef]
38. Xiao, Y.; Abbasi, N.M.; Zhu, Y.F.; Li, S.; Tan, S.J.; Ling, W.; Peng, L.; Yang, T.; Wang, L.; Guo, X.D.; et al. Layered Oxide Cathodes Promoted by Structure Modulation Technology for Sodium-Ion Batteries. *Adv. Funct. Mater.* **2020**, *30*, 1–28. [CrossRef]
39. Wang, Y.; Wang, X.; Li, X.; Yu, R.; Chen, M.; Tang, K.; Zhang, X. The Novel P3-Type Layered $Na_{0.65}Mn_{0.75}Ni_{0.25}O_2$ Oxides Doped by Non-Metallic Elements for High Performance Sodium-Ion Batteries. *Chem. Eng. J.* **2019**, *360*, 139–147. [CrossRef]
40. Amedzo-Adore, M.; Yang, J.; Han, D.; Chen, M.; Agyeman, D.A.; Zhang, J.; Zhao, R.; Kang, Y.M. Oxygen-Deficient P2-$Na_{0.7}Mn_{0.75}Ni_{0.25}O_{2-X}$ Cathode by a Reductive NH_4HF_2Treatment for Highly Reversible Na-Ion Storage. *ACS Appl. Energy Mater.* **2021**, *4*, 8036–8044. [CrossRef]
41. Yang, J.; Maughan, A.E.; Teeter, G.; Tremolet de Villers, B.J.; Bak, S.M.; Han, S.D. Structural Stabilization of P2-Type Sodium Iron Manganese Oxides by Electrochemically Inactive Mg Substitution: Insights of Redox Behavior and Voltage Decay. *ChemSusChem* **2020**, *13*, 5972–5982. [CrossRef]
42. Choi, J.; Lee, S.Y.; Yoon, S.; Kim, K.H.; Kim, M.; Hong, S.H. The Role of Zr Doping in Stabilizing $Li[Ni_{0.6}Co_{0.2}Mn_{0.2}]O_2$ as a Cathode Material for Lithium-Ion Batteries. *ChemSusChem* **2019**, *12*, 2439–2446. [CrossRef]

43. Gao, S.; Zhan, X.; Cheng, Y.T. Structural, Electrochemical and Li-Ion Transport Properties of Zr-Modified $LiNi_{0.8}Co_{0.1}Mn_{0.1}O_2$ Positive Electrode Materials for Li-Ion Batteries. *J. Power Sources.* **2019**, *410*, 45–52. [CrossRef]
44. Li, Q.; Li, Z.; Wu, S.; Wang, Z.; Liu, X.; Li, W.; Li, N.; Wang, J.; Zhuang, W. Utilizing Diverse Functions of Zirconium to Enhance the Electrochemical Performance of Ni-Rich Layered Cathode Materials. *ACS Appl. Energy Mater.* **2020**, *3*, 11741–11751. [CrossRef]
45. Yoon, C.S.; Choi, M.J.; Jun, D.W.; Zhang, Q.; Kaghazchi, P.; Kim, K.H.; Sun, Y.K. Cation Ordering of Zr-Doped $LiNiO_2$ Cathode for Lithium-Ion Batteries. *Chem. Mater.* **2018**, *30*, 1808–1814. [CrossRef]
46. Shugay, B.; Rakhymbay, L.; Konarov, A.; Myung, S.T.; Bakenov, Z. Enhanced Electrochemical Performance of Sodium Cathode Materials with Partial Substitution of Zr. *Electrochem. Commun.* **2023**, *146*, 107413. [CrossRef]
47. Kasireddy, S.R.; Gangaja, B.; Nair, S.V.; Santhanagopalan, D. Mn^{4+} Rich Surface Enabled Elevated Temperature and Full-Cell Cycling Performance of $LiMn_2O_4$ Cathode Material. *Electrochim. Acta* **2017**, *250*, 359–367. [CrossRef]
48. Döbelin, N.; Kleeberg, R. Profex: A Graphical User Interface for the Rietveld Refinement Program BGMN. *J. Appl. Crystallogr.* **2015**, *48*, 1573–1580. [CrossRef]
49. Rong, X.; Gao, F.; Ding, F.; Lu, Y.; Yang, K.; Li, H.; Huang, X.; Chen, L.; Hu, Y.S. Triple Effects of Sn-Substitution on $Na_{0.67}Ni_{0.33}Mn_{.0.67}$ O_2. *J. Mater. Sci. Technol.* **2019**, *35*, 1250–1254. [CrossRef]
50. Amine, K.; Tukamoto, H.; Yasuda, H.; Fujita, Y. A New Three-Volt Spinel $Li_{1+x}Mn_{1.5}Ni_{0.5}O_4$ for Secondary Lithium Batteries. *J. Electrochem. Soc.* **1996**, *143*, 1607–1613. [CrossRef]
51. Shaju, K.M.; Rao, S.G.V.; Chowdari, B.V.R. Performance of Layered $Li(Ni_{1/3}Co_{1/3}Mn_{1/3})O_2$ as Cathode for Li-Ion Batteries. *Electrochim. Acta.* **2002**, *48*, 145–151. [CrossRef]
52. Li, J.; Xiong, S.; Liu, Y.; Ju, Z.; Qian, Y. Uniform $LiNi_{1/3}Co_{1/3}Mn_{1/3}O_2$ Hollow Microspheres: Designed Synthesis, Topotactical Structural Transformation and Their Enhanced Electrochemical Performance. *Nano Energy* **2013**, *2*, 1249–1260. [CrossRef]
53. Han, B.; Xu, S.; Zhao, S.; Lin, G.; Feng, Y.; Chen, L.; Ivey, D.G.; Wang, P.; Wei, W. Enhancing the Structural Stability of Ni-Rich Layered Oxide Cathodes with a Preformed Zr-Concentrated Defective Nanolayer. *ACS Appl. Mater. Interfaces* **2018**, *10*, 39599–39607. [CrossRef]
54. Wan, G.; Peng, B.; Zhao, L.; Wang, F.; Yu, L.; Liu, R.; Zhang, G. Dual-strategy Modification on P2-$Na_{0.67}Ni_{0.33}Mn_{0.67}O_2$ Realizes Stable High-voltage Cathode and High Energy Density Full Cell for Sodium-ion Batteries. *SusMat* **2023**, *3*, 58–71. [CrossRef]
55. Wu, X.; Guo, J.; Wang, D.; Zhong, G.; McDonald, M.J.; Yang, Y. P2-Type $Na_{0.66}Ni_{0.33-X}Zn_xMn_{0.67}O_2$ as New High-Voltage Cathode Materials for Sodium-Ion Batteries. *J. Power Sources* **2015**, *281*, 18–26. [CrossRef]
56. Qiu, C.; He, G.; Shi, W.; Zou, M.; Liu, C. The Polarization Characteristics of Lithium-Ion Batteries under Cyclic Charge and Discharge. *J. Solid State Electrochem.* **2019**, *23*, 1887–1902. [CrossRef]
57. Xia, B.; Ye, B.; Cao, J. Polarization Voltage Characterization of Lithium-Ion Batteries Based on a Lumped Diffusion Model and Joint Parameter Estimation Algorithm. *Energies* **2022**, *15*, 1150. [CrossRef]
58. Paul, S. Materials and Electrochemistry: Present and Future Battery. *J. Electrochem. Sci. Technol.* **2016**, *7*, 115–131. [CrossRef]

Disclaimer/Publisher's Note: The statements, opinions and data contained in all publications are solely those of the individual author(s) and contributor(s) and not of MDPI and/or the editor(s). MDPI and/or the editor(s) disclaim responsibility for any injury to people or property resulting from any ideas, methods, instructions or products referred to in the content.